

The X-ray Properties of Optically Selected Clusters of Galaxies

A. K. Hicks,^{1,2*} G. W. Pratt,³ M. Donahue,² E. Ellingson,⁴ M. Gladders,⁵
H. Böhringer,⁶ H. K. C. Yee,⁷ R. Yan,⁸ J. H. Croston,⁹ and D. G. Gilbank¹⁰

¹Eureka Scientific, 2452 Delmer Street, Suite 100, Oakland, CA 94602-3017, USA

²Department of Physics & Astronomy, Michigan State University, East Lansing, MI 48824-2320, USA

³Laboratoire AIM, IRFU/Service d'Astrophysique - CEA/DSM - CNRS - Université Paris Diderot, Bât. 709,

CEA-Saclay, 91191 Gif-sur-Yvette Cedex, France

⁴Center for Astrophysics and Space Astronomy, University of Colorado at Boulder, Campus Box 389, Boulder, CO 80309, USA

⁵Department of Astronomy and Astrophysics, University of Chicago, 5640 S. Ellis Ave, Chicago, IL 60637, USA

⁶Max-Planck-Institut für extraterrestrische Physik, Giessenbachstrasse, 85748 Garching, Germany

⁷Department of Astronomy and Astrophysics, University of Toronto, 50 St. George St., Toronto, ON, M5S 3H4, Canada

⁸Department of Physics and Astronomy, University of Kentucky, 505 Rose St. Lexington, KY, 40506-0055

⁹School of Physics and Astronomy, University of Southampton, Southampton, Hampshire, SO17 1BJ, UK

¹⁰South African Astronomical Observatory, PO Box 9, Observatory 7935, South Africa

Received 2012 June

ABSTRACT

We present the results of *Chandra* and *Suzaku* X-ray observations of nine moderate-redshift ($0.16 < z < 0.42$) clusters discovered via the Red-sequence Cluster Survey (RCS). Surface brightness profiles are fitted to beta models, gas masses are determined, integrated spectra are extracted within R_{2500} , and X-ray temperatures and luminosities are inferred. The L_X - T_X relationship expected from self-similar evolution is tested by comparing this sample to our previous X-ray investigation of nine high-redshift ($0.6 < z < 1.0$) optically selected clusters. We find that optically selected clusters are systematically less luminous than X-ray selected clusters of similar X-ray temperature at both moderate and high- z . We are unable to constrain evolution in the L_X - T_X relation with these data, but find it consistent with no evolution, within relatively large uncertainties. To investigate selection effects, we compare the X-ray properties of our sample to those of clusters in the representative X-ray selected REXCESS sample, also determined within R_{2500} . We find that while RCS cluster X-ray properties span the entire range of those of massive clusters selected by other methods, their average X-ray properties are most similar to those of dynamically disturbed X-ray selected clusters. This similarity suggests that the true cluster distribution might contain a higher fraction of disturbed objects than are typically detected in X-ray selected surveys.

Key words: cosmology: observations — cosmology: large scale structure — X-rays: galaxies: clusters — galaxies: clusters: general.

1 INTRODUCTION

By virtue of their size, clusters of galaxies are an important source of information about the underlying cosmology of the universe (e.g., Allen et al. 2011, and references therein). Since the advent of the first cluster survey over 50 years ago (Abell 1958), the search for these impressive objects has grown in cosmological impact, and is currently being pursued with the ultimate objective of constraining w , the dark energy equation of state. Improved technology has enabled large-area cluster searches in several wavebands (e.g., X-ray, optical, millimetre, submm, radio) and out to formative redshifts. Consequently, the number of recent, underway, and planned cluster surveys is staggering: Böhringer et

al. 2004 (REFLEX); Valtchanov et al. 2004 (XMM-LSS); Gladders & Yee 2005 (RCS); Wester & Dark Energy Survey Collaboration 2005 (DES); Content et al. 2008 (EUCLID); Wilson et al. 2009 (SpARCS); Conconi et al. 2010 (WFXT); Vanderlinde et al. 2010 (SPT); Lloyd-Davies et al. 2011 (XCS); Marriage et al. 2011 (ACT); Planck Collaboration VIII 2011 (Planck); Predehl et al. 2011 (eROSITA); Šuhada et al. 2012 (XMM-BCS) and many more.

One overarching goal of these endeavors is to chart the evolution of the cluster mass function, thereby providing key constraints on the progression of large-scale structure formation in the universe. Constructing a mass function requires two key elements: the ability to find clusters, and an efficient method of mass estimation. Obtaining either piece necessitates an accurate understanding

* E-mail: ahicks@alum.mit.edu

Table 1. Cluster Sample

Cluster	z	l'' [h_{70}^{-1} kpc]	Telescope	obsid	Exposure [seconds]
RCS0222+0144	0.25 ^a	3.91	<i>Chandra</i>	10485	23,335
RCS1102-0319	0.33 ^b	4.75	<i>Suzaku</i>	803065010	26,381
RCS1102-0340	0.39 ^c	5.29	<i>Suzaku</i>	803064010	37,797
RCS1330+3043	0.27 ^d	4.14	<i>Chandra</i>	10487	15,824
RCS1447+0828	0.38 ^c	5.21	<i>Chandra</i>	10481	11,999
RCS1447+0949	0.20 ^a	3.30	<i>Chandra</i>	10486	17,540
RCS1615+3057	0.42 ^a	5.53	<i>Chandra</i>	10482	27,777
RCS2150-0442	0.16 ^b	2.76	<i>Chandra</i>	10488	10,506
RCS2347-3535	0.26 ^a	4.02	<i>Chandra/Suzaku</i>	10484/803057010	13,850/15,489

^a Spectroscopic (Blindert 2006)^b From X-ray spectra (this work), see text.^c Spectroscopic (Ellingson et al. 2012)^d Photometric

of relationships between the observable properties of clusters (i.e., baryons) and their underlying dark matter distributions.

The baryonic mass in clusters is dominated by the hot intra-cluster medium (ICM), therefore some of the most powerful methods of cluster identification (X-ray, SZ) use the ICM to both find clusters and estimate their masses. Several processes occur within clusters, however, that can alter the physical characteristics and distribution of cluster baryons. These include feedback (e.g., Voit & Donahue 2005), mergers (e.g., Chatzikos 2012), and radiative cooling (e.g., Pratt et al. 2009), among other non-gravitational processes (e.g., Nagai 2006). Additionally, the frequency with which those processes occur may vary with redshift (e.g., Barger et al. 2005).

Understanding the gamut of ICM properties requires X-ray observations of samples chosen independently of their X-ray characteristics. This has indeed been pursued multiple times (e.g., Holden et al. 1997; Donahue et al. 2001, 2002; Basilakos et al. 2004; Gilbank et al. 2004; Popesso et al. 2004; Sánchez et al. 2005). Most of these surveys have identified a significant population of low- L_X clusters. Unfortunately, there is a striking dearth of adequate X-ray data for these samples. Without convincing L_X and T_X measurements it is impossible to verify alternatively obtained cluster masses or investigate trends in core gas density. Due largely to this lack of quality X-ray data, concrete physical explanations for the observed scatter in cluster properties have not yet been well determined.

In our previous work (Hicks et al. 2008) we use pointed *Chandra* observations to compare the ICM properties of high- z optically selected clusters (RCS; Gladders & Yee 2005) with those of moderate-redshift X-ray selected clusters (CNOC; e.g., Yee, Ellingson, & Carlberg 1996). Our results indicate that the typical central ($\sim R_{2500}$; where $\rho_{\text{clust}}/\rho_{\text{crit}} = 2500$) gas mass fractions of the RCS sample are strikingly lower than those found in X-ray selected systems. This is also illustrated by discrepancies in the normalization of the L_X - T_X relationship between the two samples. These comparisons, however, were made between clusters of differing average redshift ($z_{\text{CNOC}} \sim 0.3$, $z_{\text{RCS}} \sim 0.8$), which were gathered via significantly different means of selection, making it difficult to disentangle the effects of selection bias from possible signatures of cluster evolution.

The main objectives of this work are to isolate these potential factors from one another and identify the cause of discrepan-

cies in ICM properties between optically and X-ray selected cluster samples. In Section 2 we introduce the present cluster sample and describe the initial processing of our *Chandra* and *Suzaku* X-ray observations. In Sections 3 and 4 we probe the surface brightness, temperature, metallicity, and density of the hot ICM present in each cluster. In Section 5 we compare the ICM properties of RCS clusters to X-ray selected samples, including the REXCESS sample for which quantities have been extracted within R_{2500} . Finally, we compare X-ray temperature to velocity dispersion for a subset of our targets (Section 6). Our results are summarized in Section 7.

Unless otherwise noted, this paper assumes a cosmology of $\Omega_M = 0.3$, $\Omega_\Lambda = 0.7$ and $H_0 = 70 \text{ km s}^{-1} \text{ Mpc}^{-1}$. All errors are quoted at 68% confidence levels.

2 CLUSTER SAMPLE & OBSERVATIONS

In an attempt to decouple the effects of sample selection from possible redshift evolution in X-ray properties, our targets were chosen to match our X-ray selected CNOC comparison sample in both redshift and mass. Velocity dispersion was used as a mass proxy for two-thirds of our targets, and initial masses for the remaining third were estimated from cluster richness (Yee & Lopez-Cruz 1999; Gladders & Yee 2005). The ranges of redshifts and velocity dispersions spanned by our sample are $0.16 < z < 0.42$ and $709 < \sigma < 1390 \text{ km s}^{-1}$, compared to CNOC ranges of $0.17 < z < 0.55$ and $575 < \sigma < 1330 \text{ km s}^{-1}$. Each target was observed in the X-ray by either *Chandra* or *Suzaku*. Table 1 lists the clusters in our sample along with their redshifts, the telescope used, obsids, and exposure times.

2.1 *Chandra* Initial Processing

Seven of our nine targets were observed with *Chandra*'s ACIS-S (Advanced CCD Imaging Spectrometer) array in VFaint mode during the period 2009 November 24 - 2010 August 3. The field of view of the ACIS-S aimpoint chip is $8' \times 8'$. *Chandra* has exceptional $0.5''$ spatial resolution, enabling very detailed investigations of cluster cores. The spectral resolution of ACIS is 120-130 eV over the energy range of interest to this study (0.3-7 keV).

Preliminary reduction of the *Chandra* data was performed as in Hicks et al. (2008). After this initial cleaning, 0.3-7.0 keV and

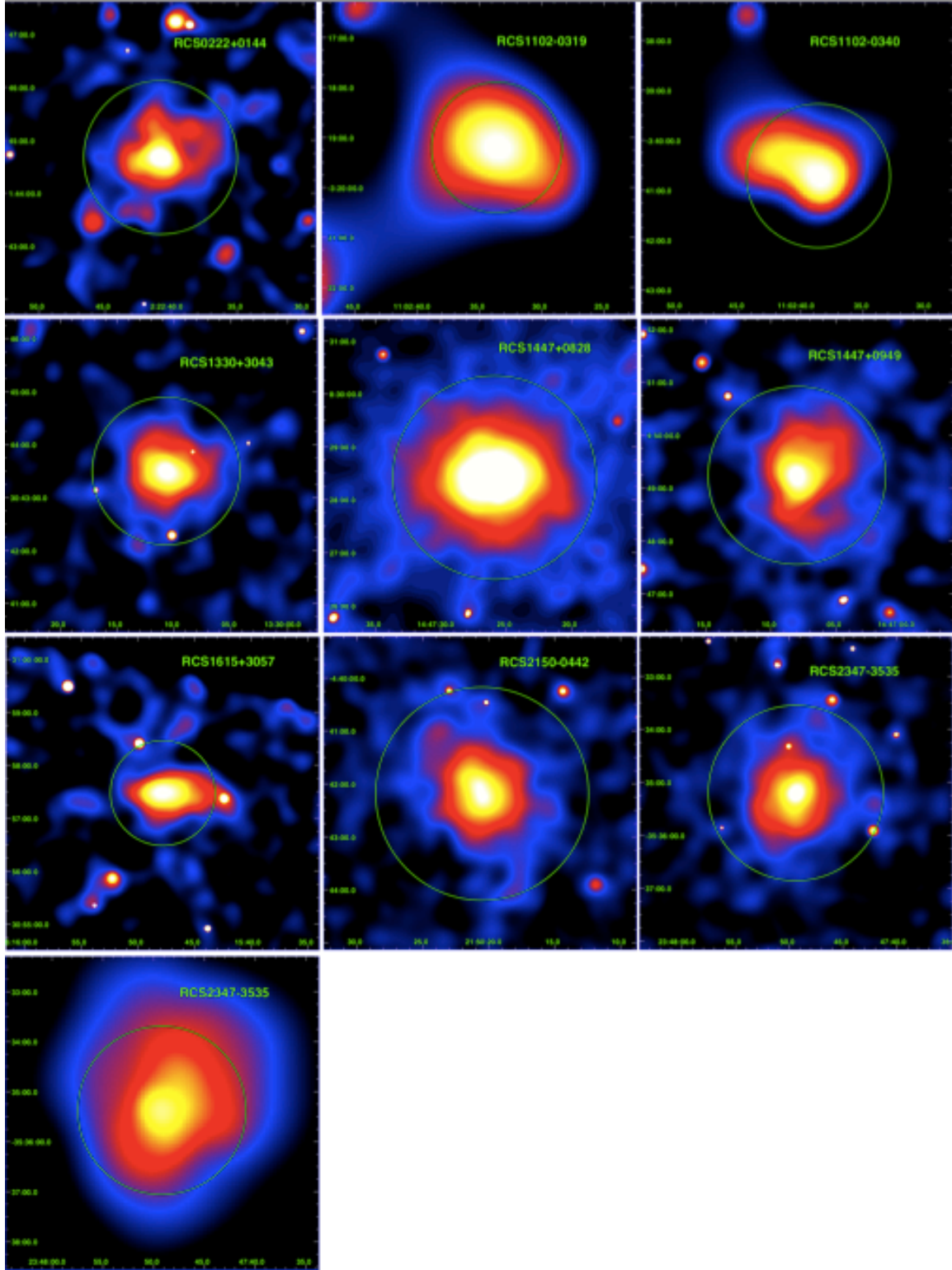


Figure 1. Smoothed Flux Images. Adaptively smoothed 0.3–7.0 keV *Chandra* flux and 0.2–12.0 keV *Suzaku* counts images of our sample. RCS1102-0319, RCS1102-0340, and the second RCS2347-3535 panel are *Suzaku* observations. Circles denote calculated values of R_{2500} for each cluster. In each image, north is up and east is to the left.

Table 2. Cluster Positions and Detection Details

Cluster	Optical Position ^a		X-ray Peak ^b		Separation [$''$]	Net Counts ^b	S/N Ratio
	RA	Dec	RA	Dec			
RCS0222+0144	02 22 40.6	+01 44 32.0	02 22 40.8	+01 44 40.3	8.8	1036	14.8
RCS1102-0319	11 02 33.0	-03 19 04.8	11 02 33.6	-03 19 12.2	11.6	2440 ^c	29.9 ^c
RCS1102-0340	11 02 39.1	-03 40 17.1	11 02 38.6	-03 40 42.7	26.7	4803 ^c	43.8 ^c
RCS1330+3043	13 30 10.7	+30 43 30.6	13 30 10.7	+30 43 30.0	0.6	926	16.2
RCS1447+0828	14 47 26.9	+08 28 17.5	14 47 25.9	+08 28 25.1	16.7	14022	112.8
RCS1447+0949	14 47 08.1	+09 49 01.7	14 47 08.0	+09 49 14.2	12.6	1531	18.7
RCS1615+3057	16 15 47.2	+30 57 18.0	16 15 47.8	+30 57 28.4	13.0	339	11.1
RCS2150-0442	21 50 19.7	-04 42 25.4	21 50 20.5	-04 42 11.2	18.6	3001	48.3
RCS2347-3535	23 47 49.2	-35 35 10.9	23 47 49.4 ^d	-35 35 12.3 ^d	2.8	2911	54.6
			23 47 49.2 ^e	-35 35 22.5 ^e	11.6	3823 ^c	60.2 ^c

^a All positions are given for equinox J2000^b 0.3-7.0 keV band, within $R < 500 h_{70}^{-1}$ kpc^c *Suzaku* observation, $R = 260''$ ^d Using *Chandra* data^e Using *Suzaku* data

0.3-2.5 keV images, instrument maps, and exposure maps were created for each dataset using the CIAO 4.2 tool MERGE_ALL and CALDB version 4.3.0. Point source detection was performed by running the tools WTRANSFORM and WRECON on the 0.3-7.0 keV flux images. Data with energies below 0.3 keV and above 7.0 keV were excluded due to uncertainties in the ACIS calibration and background contamination, respectively. These products were used solely for imaging analysis; our spectral analysis excludes all data below 0.6 keV.

2.2 *Suzaku* Initial Processing

The *Suzaku* X-ray Imaging Spectrometer (XIS) observed three of the clusters in our sample between May 31 and December 17, 2008 including one that was later observed by *Chandra* (RCS2347-3535). *Suzaku*'s field of view is $18' \times 18'$, and it has a spatial resolution of only $\sim 2'$. One of the advantages of *Suzaku*, however, is its excellent low-energy spectral resolution (60 eV at 0.25 keV).

Suzaku data were reprocessed to include the most recent calibration files using the HEASOFT 6.9 *Suzaku* software Version 16 tool AEPIPELINE. Calibration sources were removed from the data using XSELECT, and data from XIS0, XIS1, and XIS3 were combined to produce integrated images in the 0.2-12.0 keV energy range.

3 IMAGES AND SURFACE BRIGHTNESS PROFILE MODELLING

3.1 Images and cluster centers

Figure 1 contains smoothed 0.3-7.0 keV *Chandra* flux and 0.2-12.0 keV *Suzaku* counts images of each of the clusters in our sample (produced by the CIAO tool CSMOOTH). Using these images we determined the location of the X-ray emission peak of each cluster. Optical positions were taken from RCS cluster catalogs, which were computed from the smoothed galaxy distribution used for cluster identification (see Gladders & Yee 2005, for details). *Suzaku* observations were included in this exercise despite having $\sim 2'$ spatial resolution. All clusters were found within $27''$ of their optical positions, and all *Chandra* observed clusters were found

within $19''$, with a mean offset of $10.4''$. Table 2 lists optical positions, X-ray positions, net counts ($C - B$) and signal-to-noise ratios derived from the method described in Appendix A. All clusters are detected at high significance. The median number of source counts per observation is 2911, with values ranging between 339 (RCS1615+3057) and 14,022 (RCS1447+0828).

3.2 Surface Brightness Profiles

Radial surface brightness profiles were extracted in circular annuli from both targeted observations and blank sky background files using 0.3-2.5 keV *Chandra* counts images. The cluster profiles were binned to ensure $S/N > 3$ in each bin and background-subtracted. None of our surface brightness bins are narrower than $1''$, therefore we do not expect to see any effects from *Chandra*'s $0.5''$ FWHM PSF on our profiles.

The surface brightness profiles were fitted to a beta-model:

$$I(r) = I_0 \left(1 + \frac{r^2}{r_c^2} \right)^{-3\beta + \frac{1}{2}}, \quad (1)$$

where I_0 is the normalization and r_c is the core radius. We compared the measured surface brightness (with error bars computed from photon statistics) to the average model surface brightness integrated within each radial bin while performing a Levenberg-Marquardt least-squares fit to the model, as implemented in the IDL routine `mpcurvefit`¹.

Best fitting model parameters for the seven *Chandra*-observed clusters are given in Table 3, and images of these fits are shown in Figure B1. Though many of the clusters exhibit some substructure, most were reasonably well fitted by the β model (see Table 3 for goodness of fit data). β values for our sample are generally lower than the typical value of $2/3$ (Neumann & Arnaud 1999), with a sample average of 0.42 ± 0.01 , suggesting that the gas is less centrally-concentrated in these targets compared to those studied by Neumann & Arnaud (1999).

RCS2347-3535 contains a region of excess emission in its central 10-20 kpc, suggesting that it may harbour a small cool core.

¹ Available courtesy Craig B. Markwardt, <http://cow.physics.wisc.edu/craigm/idl/idl.html>

Table 4. Spectral Fits ($\Delta = 2500$)

Cluster	z	N_H [10^{20} cm^{-2}]	kT [keV]	Z [Z_\odot]	Norm [10^{-4} cm^{-5}]	$n_{e,0}$ [10^{-3} cm^{-3}]
RCS0222+0144	0.25	3.30	$4.6^{+0.9}_{-0.8}$	$1.4^{+0.9}_{-0.6}$	$1.7^{+0.3}_{-0.3}$	$4.4^{+0.3}_{-0.4}$
RCS1102-0319 ^a	$0.334^{+0.007}_{-0.007}$	4.04	$4.3^{+0.5}_{-0.4}$	$0.5^{+0.2}_{-0.2}$	$3.7^{+0.3}_{-0.3}$...
RCS1102-0340 ^a	0.39	4.06	$6.3^{+0.7}_{-0.7}$	$0.2^{+0.1}_{-0.1}$	$5.8^{+0.2}_{-0.2}$...
RCS1330+3043	0.27	1.16	$4.4^{+1.0}_{-0.9}$	$0.3^{+0.3}_{-0.3}$	$3.6^{+0.5}_{-0.5}$	$8.9^{+0.6}_{-0.4}$
RCS1447+0828	0.38	2.24	$6.8^{+0.3}_{-0.2}$	$0.38^{+0.06}_{-0.05}$	101^{+1}_{-1}	161^{+1}_{-1}
(Core-excised) ^b	...	2.24	13^{+3}_{-2}	$0.4^{+0.3}_{-0.2}$	24^{+1}_{-1}	...
RCS1447+0949	0.20	1.83	$2.4^{+0.3}_{-0.3}$	$0.02^{+0.09}_{-0.02}$	$6.8^{+0.5}_{-0.5}$	$7.7^{+0.3}_{-0.3}$
RCS1615+3057	0.42	2.6	$3.8^{+1.0}_{-0.9}$	$0.0^{+0.1}_{-0.1}$	$1.7^{+0.1}_{-0.2}$	$5.5^{+0.2}_{-0.3}$
RCS2150-0442	$0.160^{+0.008}_{-0.015}$	2.72	$3.6^{+0.4}_{-0.3}$	$0.4^{+0.2}_{-0.1}$	$11.6^{+0.6}_{-0.5}$	$8.2^{+0.2}_{-0.3}$
RCS2347-3535 ^c	0.26	1.22	$4.9^{+0.3}_{-0.3}$	$0.49^{+0.10}_{-0.09}$	$7.3^{+0.3}_{-0.3}$	$5.9^{+0.1}_{-0.1}$
RCS2347-3535 ^e	...	1.22	$5.3^{+0.7}_{-0.7}$	$0.5^{+0.3}_{-0.2}$	$7.3^{+0.4}_{-0.5}$	$5.9^{+0.1}_{-0.1}$
(Core-excised) ^{b,e}	...	1.22	$4.9^{+1.3}_{-0.8}$	$0.08^{+0.32}_{-0.08}$	$4.7^{+0.3}_{-0.4}$...
RCS2347-3535 ^{a,f}	...	1.22	$4.7^{+0.3}_{-0.3}$	$0.5^{+0.1}_{-0.1}$	$11.5^{+0.4}_{-0.4}$...

^a *Suzaku* observation, $R = 260''$ ^b Central $0.15 R_{500}$ removed from spectrum.^c Best simultaneous fit to *Chandra* and *Suzaku* spectra.^d *Chandra* normalization; *Suzaku* normalization for this fit is $11.5^{+0.4}_{-0.4} \times 10^{-4} \text{ cm}^{-5}$.^e Using only *Chandra* data.^f Using only *Suzaku* data.**Table 3.** β -Model Fits

Cluster	r_c [kpc]	β	l_0 ¹	Outermost Bin [kpc] ²	χ^2/DOF
RCS0222+0144	24 ± 13	0.32 ± 0.02	2.0 ± 0.7	276-297	11.0/11
RCS1330+3043	30 ± 8	0.39 ± 0.02	5 ± 1	286-366	28.3/28
RCS1447+0828	28.9 ± 0.8	0.581 ± 0.003	820 ± 20	836-875	135.6/116
RCS1447+0949	30 ± 7	0.36 ± 0.01	4.4 ± 0.7	450-515	40.6/52
RCS1615+3057	37 ± 22	0.34 ± 0.04	1.8 ± 0.6	235-276	6.5/8
RCS2150-0442	55 ± 6	0.51 ± 0.02	9.1 ± 0.8	370-411	63.8/64
RCS2347-3535	70 ± 12	0.45 ± 0.02	5.1 ± 0.6	454-476	53.2/53

None of the other clusters in our sample exhibit a significant central surface brightness excess above the β model.

4 SPECTROSCOPY

4.1 Initial spectral fits and redshift estimates

Initial spectra were extracted from each point-source-removed event file in a circular region with a $300 h_{70}^{-1} \text{ kpc}$ radius (*Chandra*) or $260''$ radius (*Suzaku*). These values were chosen to provide an initial spectrum with as close to an R_{2500} extraction radius as possible. In the case of *Suzaku* observations, the smallest recommended radius for extracting spectral data is $260''$. Individual spectra were extracted from each *Suzaku* XIS CCD and fitted simultaneously.

All spectra were analyzed in XSPEC (Arnaud 1996), using weighted response matrices (RMFs) and effective area files (ARFs) generated with the CIAO tool SPECEXTRACT (*Chandra*), and XISRMFGEN and XISSIMARFGEN (*Suzaku*). For the *Chandra* observations, blank sky backgrounds were renormalized to match the 9.5-12.0 keV count rates of each exposure, then extracted in identical regions as source spectra. *Suzaku* backgrounds were compiled from the remaining data after calibration sources, point sources, and the target cluster were removed.

Spectra were fitted with single temperature spectral models, inclusive of foreground absorption, using Cash statistics (Cash 1979). Each spectrum was fitted with the absorbing column frozen at its measured value (Dickey & Lockman 1990). Metal abundances were allowed to vary. Data with energies below 0.6 keV and above

7.0 keV were excluded from the *Chandra* fits, while *Suzaku* spectra were fitted in the 0.5-8.0 keV energy range (e.g., Bautz et al. 2007).

Redshifts were fitted for the three clusters in our sample that do not have spectroscopic measurements. We were unable to constrain a redshift for RCS1330+3043, and therefore use its photometric redshift ($z = 0.27$) in further analysis. The fits of the other two clusters resulted in $z = 0.334 \pm 0.007$ for RCS1102-0319, and $z = 0.160^{+0.008}_{-0.015}$ for RCS2150-0442, within 7% and 20% (respectively) of photometric redshift estimates obtained using the color of the red sequence (e.g., Gladders & Yee 2005). Fits with redshift fixed at these values were used in subsequent analysis (Table 4). The small uncertainties in these values ($\leq 10\%$) do not substantially affect our analysis.

A core-removed ($0.15 R_{500}$) spectrum was extracted and fitted for RCS1447+0828, indicating that it possesses a strong cool core, with an integrated temperature of $6.8^{+0.3}_{-0.2} \text{ keV}$ and core-removed temperature $T_X = 13^{+3}_{-2} \text{ keV}$ (Table 4). Due to the central excess in its surface brightness profile, a core-excised spectrum was also fitted for RCS2347-3535; however, no conclusive evidence for soft central emission was found in this case.

4.2 Scaled aperture estimate

With an average of only 3000 counts per target, we do not have sufficient signal to undertake a full hydrostatic mass analysis, or even fit core-excised spectra out to R_{500} . Due to the shallow nature of our observations, we choose R_{2500} as the fiducial radius for our measurements.

We employ scaling relations in order to estimate R_{2500} . The present sample contains objects in a variety of dynamical states and thus it is essential to use an appropriate scaling relation. We measure R_{2500} for our *Chandra* observations using $Y_X (\equiv M_g T_X)$ as a mass proxy. The decision to use Y_X was motivated by two principal factors. Firstly, the simulations of Kravtsov et al. (2006) indicate that Y_X is a robust mass proxy even in the presence of significant dynamical activity. Secondly, use of Y_X facilitates compar-

Table 5. Sample quantities estimated within R_{2500} .

Cluster	$M-Y_X$					$M-T_X$				
	R_{2500} [kpc]	M_{tot} [$10^{14} M_{\odot}$]	M_g [$10^{13} M_{\odot}$]	f_{gas}	L_X [$10^{44} \text{ erg s}^{-1}$]	R_{2500} [kpc]	M_{tot} [$10^{14} M_{\odot}$]	M_g [$10^{13} M_{\odot}$]	f_{gas}	L_X [$10^{44} \text{ erg s}^{-1}$]
RCS0222+0144	346 $^{+14}_{-13}$	0.75 $^{+0.09}_{-0.09}$	0.25 $^{+0.02}_{-0.02}$	0.032 $^{+0.005}_{-0.005}$	0.5 $^{+0.2}_{-0.2}$	423 $^{+42}_{-37}$	1.4 $^{+0.4}_{-0.4}$	0.38 $^{+0.03}_{-0.03}$	0.027 $^{+0.008}_{-0.008}$	0.5 $^{+0.4}_{-0.1}$
RCS1102-0319 ^a	387 $^{+27}_{-23}$	1.2 $^{+0.3}_{-0.2}$	1.7 $^{+0.5}_{-0.4}$
RCS1102-0340 ^a	457 $^{+26}_{-26}$	2.1 $^{+0.4}_{-0.4}$	3.4 $^{+0.5}_{-0.3}$
RCS1330+3043	370 $^{+17}_{-15}$	1.0 $^{+0.1}_{-0.1}$	0.48 $^{+0.03}_{-0.02}$	0.049 $^{+0.007}_{-0.006}$	1.1 $^{+0.4}_{-0.3}$	405 $^{+46}_{-42}$	1.3 $^{+0.4}_{-0.4}$	0.57 $^{+0.04}_{-0.03}$	0.04 $^{+0.01}_{-0.01}$	1.2 $^{+0.4}_{-0.3}$
RCS1447+0828 ^b	611 $^{+22}_{-22}$	4.8 $^{+0.7}_{-0.5}$	5.00 $^{+0.04}_{-0.04}$	0.10 $^{+0.01}_{-0.01}$	61 $^{+3}_{-3}$	661 $^{+79}_{-55}$	6 $^{+2}_{-2}$	5.6 $^{+0.9}_{-1.3}$	0.09 $^{+0.03}_{-0.03}$	62 $^{+4}_{-4}$
RCS1447+0949	338 $^{+10}_{-10}$	0.67 $^{+0.06}_{-0.06}$	0.40 $^{+0.02}_{-0.02}$	0.060 $^{+0.006}_{-0.006}$	0.7 $^{+0.2}_{-0.1}$	314 $^{+21}_{-21}$	0.5 $^{+0.1}_{-0.1}$	0.35 $^{+0.01}_{-0.01}$	0.07 $^{+0.01}_{-0.01}$	0.7 $^{+0.1}_{-0.2}$
RCS1615+3057	334 $^{+17}_{-16}$	0.8 $^{+0.1}_{-0.1}$	0.39 $^{+0.01}_{-0.02}$	0.047 $^{+0.007}_{-0.007}$	0.9 $^{+0.2}_{-0.2}$	349 $^{+46}_{-42}$	0.9 $^{+0.4}_{-0.3}$	0.42 $^{+0.01}_{-0.02}$	0.05 $^{+0.02}_{-0.02}$	0.8 $^{+0.4}_{-0.1}$
RCS2150-0442	361 $^{+9}_{-8}$	0.79 $^{+0.06}_{-0.05}$	0.48 $^{+0.01}_{-0.02}$	0.061 $^{+0.005}_{-0.005}$	1.4 $^{+0.2}_{-0.2}$	393 $^{+22}_{-17}$	1.0 $^{+0.2}_{-0.1}$	0.80 $^{+0.07}_{-0.09}$	0.055 $^{+0.01}_{-0.006}$	1.4 $^{+0.3}_{-0.2}$
RCS2347-3535	406 $^{+7}_{-7}$	1.24 $^{+0.06}_{-0.06}$	0.73 $^{+0.01}_{-0.02}$	0.059 $^{+0.003}_{-0.003}$	2.0 $^{+0.4}_{-0.4}$	434 $^{+14}_{-14}$	1.5 $^{+0.1}_{-0.1}$	0.82 $^{+0.02}_{-0.02}$	0.055 $^{+0.004}_{-0.004}$	2.1 $^{+0.4}_{-0.4}$

^a *Suzaku* observation, $L_{X,2500}$ estimated within aperture of radius $R = 260''$.

^b Core-excised temperature used to determine R_{Δ} .

ison of our optically selected sample to the X-ray selected REXCESS sample, since REXCESS uses Y_X exclusively.

We used an iterative process to estimate the cluster masses. First we calculated central densities using the β model parameters from Sect. 3.2 and initial spectral fits described in Sect. 4.1:

$$n_{e,0}^2 = \frac{4\pi d_{\text{ang}}^2 (1+z)^2 K 10^{14}}{0.82 4\pi r_c^3 EI} \text{ cm}^{-6} \quad (2)$$

(Ettori, Tozzi & Rosati 2003). Here K is the normalization of the XSPEC model and EI is the emission integral, estimated by integrating the (spherical) emission from the source out to 10 Mpc (see Ettori, Tozzi & Rosati 2003, for details). Values of $n_{e,0}$ were then used to determine total gas mass by integrating the cluster density profile out to R_{500} :

$$\rho_{\text{gas}}(r) = \rho_0 \left[1 + \frac{r^2}{r_c^2} \right]^{-3\beta/2}, \quad (3)$$

where $\rho_0 = n_{e,0} \mu_e m_p$, and $\mu_e = 1.17$. We then use the $M-Y_X$ relation of Arnaud, Pointecouteau, & Pratt (2007) to estimate the mass and radius of each object. The Arnaud, Pointecouteau, & Pratt (2007) $M-Y_X$ relation uses $T[0.15-0.75 R_{500}]$ as well as $M_g[R_{500}]$. We translate our $T[R_{2500}]$ measurements to $T[0.15-0.75 R_{500}]$ using the mean $T[R_{2500}]/T[0.15-0.75 R_{500}]$ ratio from the REXCESS sample. R_{500} was then converted to R_{2500} using the simple relationship $R_{2500} = 0.44 R_{500}$ (Arnaud, Pointecouteau, & Pratt 2005)². The process of extracting spectra, fitting temperatures, determining gas mass, and re-estimating the mass and radius R_{2500} was repeated until the radius values converged.

Given the lower spatial resolution of *Suzaku*, in these cases we instead determined R_{2500} using the $M-T_X$ relationship of Arnaud, Pointecouteau, & Pratt (2005). The cluster RCS2347-3535 has been observed by both *Chandra* and *Suzaku*. Here *Chandra* spatial information was used in tandem with combined temperature fitting of both *Chandra* and *Suzaku* spectra. To confirm that the larger extraction region of *Suzaku* was not impacting best fitting temperatures, *Chandra* and *Suzaku* spectra were also fitted individually. All values of T_X (including the core-excised value) are consistent with one another within 1σ errors.

² Use of a constant R_{2500}/R_{500} ratio assumes that a constant concentration. This is a fair assumption given the mass range of interest (see e.g., Pointecouteau et al. 2005).

4.3 Scaled quantities

Table 5 lists total gravitating masses (M_{tot}), gas masses (M_g), gas mass fractions (f_{gas}), and temperatures (T_X) within R_{2500} . Total gravitating masses estimated from the scaling relationships $M-T_X$ and $M-Y_X$ were found to be in statistical agreement with one another, with a slight tendency for the latter to be smaller.

Bolometric (unabsorbed 0.01-100 keV) luminosities $L_X[R_{2500}]$ were calculated by extrapolating the best fit spectrum within XSPEC. Error bars on L_X take into account uncertainties in R_{2500} , temperature, abundance, and spectral normalization. To investigate whether different methods of determining R_{2500} have a significant effect on resulting L_X-T_X relationships, we also calculate R_{2500} for the *Chandra* clusters using $M-T_X$ (Arnaud, Pointecouteau, & Pratt 2005), and re-extract spectra at those radii to obtain additional luminosities. We find that even when R_{2500} values differ by 20%, measured luminosities do not change appreciably (Table 5). Since we do not expect T_X to change drastically on ~ 50 kpc scales at radii $R \geq R_{2500}$, we find that L_X-T_X relationships are robust to different methods of determining R_{2500} .

5 CLUSTER SAMPLE COMPARISONS

5.1 Context and comparison samples

In our previous work (Hicks et al. 2008) we found that high-redshift, optically selected clusters had noticeably different X-ray properties than our moderate-redshift, X-ray selected comparison sample (CNOC). With our current moderate- z optically selected sample we are in a position to confirm whether these differences are due primarily to selection bias or to redshift evolution in cluster properties. We use the following comparison samples:

- Ten high-redshift ($0.6 < z < 1.0$) optically selected RCS clusters selected from among the optically-richest of the 6,483 candidates detected in the first 90 deg² of the RCS (Gladders & Yee 2005). The *Chandra* X-ray observations of these clusters are presented in Hicks et al. (2008).
- Fourteen moderate-redshift ($0.2 < z < 0.55$) X-ray selected CNOC clusters. This sample (Yee, Ellingson, & Carlberg 1996) is derived from detections in the *Einstein Observatory* Extended Medium-Sensitivity Survey (EMSS Gioia et al. 1990). CNOC

was originally chosen as a comparison sample because it has been extensively observed in optical, with galaxy redshifts of ~ 1200 cluster members as well as detailed photometric catalogues available (e.g., Yee et al. 1996). It is not, however, necessarily representative of X-ray selected samples as a whole. As the highest-luminosity clusters from the X-ray flux-limited, wide-area EMSS survey, the CNOC sample is almost certainly drawn from the extreme X-ray bright tail of the cluster distribution. The *Chandra* X-ray observations of these clusters are detailed in Hicks et al. (2006).

- Thirty-one clusters from the REXCESS sample (Böhringer et al. 2007). REXCESS provides homogenous coverage of the luminosity range $0.4 - 20 \times 10^{44} \text{ h}_{50}^{-2} \text{ erg s}^{-1}$ in the 0.1-2.4 keV band ($T_X \geq 2 \text{ keV}$) over the redshift range $0.055 < z < 0.183$. It is representative of the X-ray selected population, clusters having been selected in X-ray luminosity only, without regard for any other characteristic (apart from angular size, so that they would fit into the field of view of *XMM-Newton*). The X-ray scaling properties of the REXCESS sample within R_{500} are discussed in Pratt et al. (2009). For the present paper, we have recalculated the X-ray temperatures and bolometric luminosities within R_{2500} defined as in Sect. 4.2 above. The resulting R_{2500} , T_X , L_X , f_{gas} , values are listed in Table 6. We also list the cool core (cc) and morphological classifications (Pratt et al. 2009). Objects are classed as cool core if central density $E(z)^{-2} n_{e,0} > 4 \times 10^{-2} \text{ cm}^{-3}$. Objects are classified as morphologically disturbed if the centroid shift parameter ³ $\langle w \rangle > 0.01 R_{500}$. The remaining systems are neither cool core nor morphologically disturbed.

(Böhringer et al. 2010)

5.2 Density Profiles

Using the β -model fits given in Table 3 and central densities found in Table 4, radial density profiles were produced, scaled by R_{500} , and compared to those of the REXCESS sample. The left hand panel of Figure 2 shows a comparison between the scaled density profiles of the moderate-redshift RCS and REXCESS samples. On average the scaled profiles of the RCS clusters are suppressed in the central regions compared to REXCESS. Note that this is a strong effect, reaching out well beyond R_{2500} . RCS1447 is included in the calculation of the mean profile. Excluding it from the calculation would further suppress the average scaled density profile of the RCS systems in the central regions.

The middle panel of Figure 2 shows the RCS clusters compared to the non-cool-core REXCESS subset only. Once again, there is a clear offset in the average density profile that extends out well beyond R_{2500} .

The right hand panel of Fig. 4 shows the RCS clusters compared to the morphologically disturbed REXCESS subsample. Here the agreement between mean scaled density profiles is actually quite remarkable. Note that there are two cool-core systems in the REXCESS morphologically disturbed subset, just as there is a cool core in the RCS moderate- z sample (RCS1447), thus both samples span the whole range of cluster properties. Also, the mass

ranges of the two samples match quite well, and this good agreement in mass is reflected in the similar temperature range. Therefore this effect is not likely to be the result of variations in gas mass fraction with mass.

5.3 The $L_X - T_X$ Relationship

Studying the relationships between global cluster properties (L_X , T_X , M_{tot} , etc.) over a broad range in redshift allows us to investigate the influence of non-gravitational processes on cluster formation and evolution. In addition, these relationships give us insight regarding cluster dynamical state and composition, as well as provide ready methods of comparison between different cluster samples. In this work we focus primarily on X-ray temperature (T_X) and luminosity (L_X), since they are tied most closely to the actual data and require fewer assumptions than extrapolated properties such as total cluster mass. To facilitate comparisons between optically selected and X-ray selected clusters, we make use of our previous *Chandra* analyses of the CNOC (Hicks et al. 2006) and high- z RCS samples (Hicks et al. 2008).

In all $L_X - T_X$ relationships, L_X has been scaled by the cosmological factor $E_z = H(z)/H_0 = [\Omega_m(1+z)^3 + \Omega_\Lambda]^{1/2}$ and the relationship has been fitted with the form

$$\log_{10} (E_z^{-1} L_X) = C1 + C2 \log_{10} T_X, \quad (4)$$

with T_X in units of 5 keV and L_X in units of $10^{44} \text{ erg s}^{-1}$. New best fitting relationships are determined using both the bisector and orthogonal modifications of the BCES algorithm in Akritas & Ber-shady (1996), with figures displaying bisector fits for ease of comparison to our previous work.

It is immediately clear from visual inspection of Figure 3a that our current targets are overall less luminous for a given temperature than the CNOC sample, in keeping with our previously-observed RCS sample. This result suggests that global discrepancies between the X-ray properties of X-ray and optically selected cluster samples are wholly attributable to selection bias.

After correcting for self-similar evolution we find no convincing evidence of redshift evolution in cluster properties within the complete X-ray observed RCS sample ($0.15 < z < 1.0$). To further explore this point, we fitted the RCS moderate- z and high- z samples together with the function

$$\log_{10} (L_X) = A \log_{10} (E_z/1.3) + B \log_{10} (T_X/5) + C \quad (5)$$

The best fitting values are (bootstrap uncertainties): $A = 0.43 \pm 1.15$; $B = 2.69 \pm 0.84$; and $C = 3.23 \pm 1.24$, showing that we are quantitatively unable to constrain evolution with the current sample.

Figure 3b shows RCS and REXCESS $L_X - T_X$ scaling relationships, for the entire REXCESS sample and for just the non-cool-core (ncc) clusters. For the REXCESS sample, cool cores define the upper envelope of the relation while morphologically disturbed systems define the lower envelope. The vast majority of the dispersion comes from the cool cores. While REXCESS cool-core clusters look much like the high- L_X CNOC sample, the non-cool-core clusters are situated similarly to the optically selected sample.

It is clear that the normalization, in particular, that one will obtain for any $L_X - T_X$ fit will depend strongly on the sample composition. Note also that the intrinsic dispersion about the REXCESS $L_X - T_X$ relation is considerably larger than the 70% dispersion about the $L_X - T_X$ relation for quantities measured within

³ The centroid shift parameter is defined as the standard deviation of the projected separations between the X-ray peak and the centroid at each radius in the $[0.1-1] R_{500}$ region (see e.g., Pratt et al. 2009; Böhringer et al. 2010)

Table 6. REXCESS X-ray Properties at R_{2500}

Cluster	z	R_{2500} [h_{70}^{-1} kpc]	T_X [keV]	L_X [10^{44} erg s $^{-1}$]	f_{gas}	CC	Disturbed
RXC J0003+0203	0.0924	388.3	$4.24^{+0.07}_{-0.07}$	$1.64^{+0.01}_{-0.01}$	0.072		
RXC J0006-3443	0.1147	469.1	$5.7^{+0.2}_{-0.2}$	$3.00^{+0.04}_{-0.04}$	0.068		✓
RXC J0020-2542	0.1410	462.9	$6.3^{+0.1}_{-0.1}$	$5.98^{+0.03}_{-0.03}$	0.095		
RXC J0049-2931	0.1084	357.7	$3.9^{+0.2}_{-0.2}$	$1.68^{+0.02}_{-0.02}$	0.082		
RXC J0145-5300	0.1168	482.4	$5.8^{+0.1}_{-0.1}$	$3.86^{+0.03}_{-0.03}$	0.074		✓
RXC J0211-4017	0.1008	303.4	$2.20^{+0.03}_{-0.03}$	$0.688^{+0.005}_{-0.005}$	0.075		
RXC J0225-2928	0.0604	307.3	$2.49^{+0.09}_{-0.09}$	$0.417^{+0.004}_{-0.004}$	0.055		✓
RXC J0345-4112	0.0603	304.9	$2.36^{+0.04}_{-0.05}$	$0.701^{+0.005}_{-0.005}$	0.068	✓	
RXC J0547-3152	0.1483	502.1	$6.7^{+0.1}_{-0.1}$	$7.87^{+0.04}_{-0.04}$	0.091		
RXC J0605-3518	0.1392	463.2	$4.58^{+0.04}_{-0.04}$	$8.67^{+0.04}_{-0.04}$	0.102	✓	
RXC J0616-4748	0.1164	415.9	$4.45^{+0.09}_{-0.09}$	$1.74^{+0.02}_{-0.02}$	0.065		✓
RXC J0645-5413	0.1644	566.9	$7.3^{+0.1}_{-0.1}$	$15.9^{+0.1}_{-0.1}$	0.099		
RXC J0821+0112	0.0822	334.8	$3.3^{+0.1}_{-0.1}$	$0.650^{+0.008}_{-0.008}$	0.063		
RXC J0958-1103	0.1669	477.1	$5.6^{+0.3}_{-0.3}$	$11.0^{+0.1}_{-0.1}$	0.107	✓	
RXC J1044-0704	0.1342	412.7	$3.49^{+0.02}_{-0.02}$	$6.91^{+0.02}_{-0.02}$	0.112	✓	
RXC J1141-1216	0.1195	392.0	$3.44^{+0.03}_{-0.03}$	$3.36^{+0.01}_{-0.01}$	0.087	✓	
RXC J1236-3354	0.0796	333.7	$2.82^{+0.03}_{-0.03}$	$0.866^{+0.006}_{-0.006}$	0.068		
RXC J1302-0230	0.0847	372.9	$3.43^{+0.04}_{-0.04}$	$1.107^{+0.007}_{-0.007}$	0.060	✓	✓
RXC J1311-0120	0.1832	584.2	$9.17^{+0.07}_{-0.07}$	$33.78^{+0.07}_{-0.07}$	0.116	✓	
RXC J1516+0005	0.1181	438.4	$5.21^{+0.07}_{-0.07}$	$3.59^{+0.02}_{-0.02}$	0.083		
RXC J1516-0056	0.1198	410.5	$4.23^{+0.09}_{-0.09}$	$1.60^{+0.01}_{-0.01}$	0.062		✓
RXC J2014-2430	0.1538	511.6	$4.80^{+0.04}_{-0.04}$	$19.33^{+0.06}_{-0.06}$	0.110	✓	
RXC J2023-2056	0.0564	327.5	$3.24^{+0.08}_{-0.08}$	$0.528^{+0.006}_{-0.006}$	0.059		✓
RXC J2048-1750	0.1475	477.4	$5.3^{+0.1}_{-0.1}$	$3.63^{+0.03}_{-0.03}$	0.074		✓
RXC J2129-5048	0.0796	398.8	$4.2^{+0.1}_{-0.1}$	$1.02^{+0.01}_{-0.01}$	0.056		✓
RXC J2149-3041	0.1184	392.6	$3.31^{+0.03}_{-0.03}$	$3.10^{+0.01}_{-0.01}$	0.083	✓	
RXC J2157-0747	0.0579	332.8	$3.27^{+0.08}_{-0.08}$	$0.294^{+0.003}_{-0.003}$	0.041		✓
RXC J2217-3543	0.1486	452.9	$5.38^{+0.08}_{-0.08}$	$5.31^{+0.02}_{-0.02}$	0.090		
RXC J2218-3853	0.1411	500.5	$6.0^{+0.1}_{-0.1}$	$8.27^{+0.02}_{-0.02}$	0.095		✓
RXC J2234-3744	0.1510	568.3	$8.6^{+0.1}_{-0.1}$	$17.03^{+0.08}_{-0.08}$	0.108		
RXC J2319-7313	0.0984	349.3	$2.20^{+0.03}_{-0.03}$	$1.69^{+0.01}_{-0.01}$	0.080	✓	✓

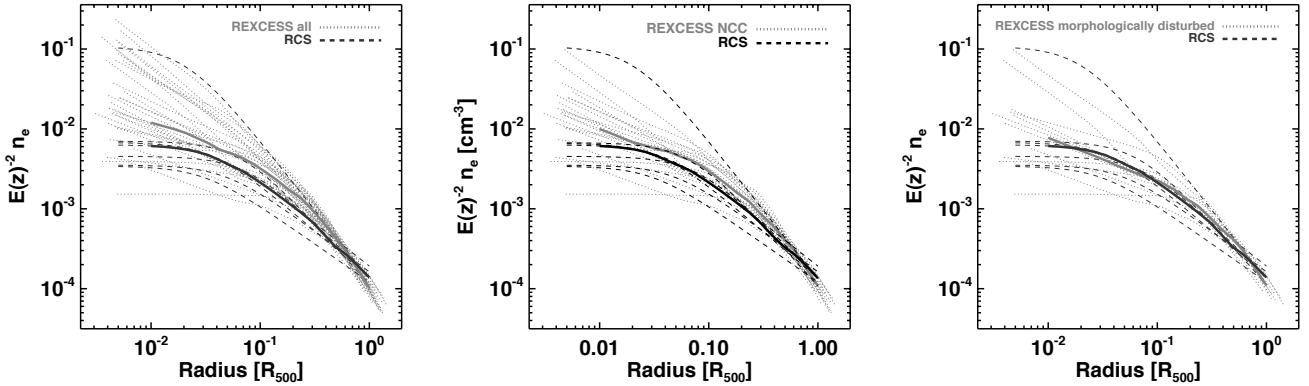


Figure 2. Density Profiles Moderate redshift RCS (dashed) vs REXCESS (dotted) density profiles, including mean density profiles for each sample (solid lines). *Figure 2a:* RCS vs full REXCESS sample. The density profiles of the RCS clusters are on average flatter in their central regions than the REXCESS systems, but are in good agreement with the X-ray systems at large radii ($\sim R_{500}$). *Figure 2b:* RCS vs non-cool-core REXCESS systems only, also exhibiting a slight offset. *Figure 2c:* RCS vs REXCESS morphologically disturbed subsample only. Here the mean profiles of the two samples are essentially identical.

R_{500} (Pratt et al. 2009). The larger dispersion we see is due to measuring quantities in the core regions, where the variation in density is strongest.

Building on the results of Section 5.2, we compare REXCESS morphologically disturbed clusters to the RCS sample (Figure 3c). Here we find an even closer similarity in X-ray properties, to the extent that even best-fitting relationships lie nearly on top

of one another. This result is expected given the agreement in gas density profiles between our targets and the REXCESS morphologically disturbed subsample. L_X - T_X fits for a variety of sample combinations are reported in Table 7.

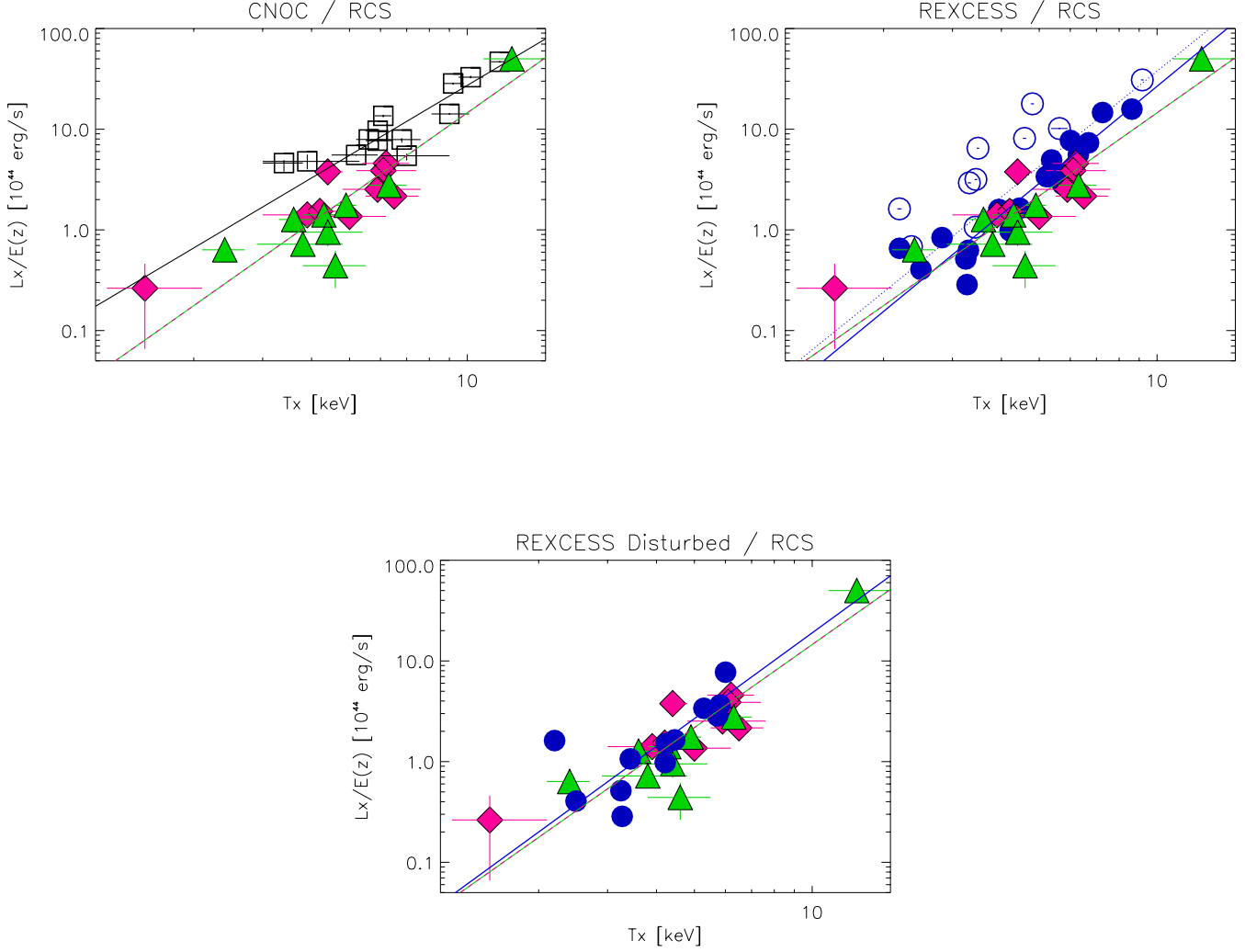


Figure 3. L_X - T_X Relationships. X-ray temperatures are plotted against cosmologically consistent, intrinsic bolometric luminosities within R_{2500} . In all panels diamonds represent high- z RCS clusters ($z_{\text{avg}} = 0.80$), triangles denote the current sample ($z_{\text{avg}} = 0.30$), and the dashed line shows the L_X - T_X relationship for the entire X-ray observed RCS sample. *Figure 3a:* Squares designate moderate redshift CNOC clusters ($z_{\text{avg}} = 0.32$), and the solid line shows their best fitting relationship. As in [Hicks et al. \(2008\)](#), the X-ray selected sample exhibits a higher normalization than optically selected clusters. *Figure 3b:* Circles represent the REXCESS sample. Here the solid line shows the fit to non-cool-core REXCESS clusters (filled circles) and the dotted line is the best fit to the entire REXCESS sample. Open circles denote cool-core clusters. *Figure 3c:* Here circles show only the disturbed REXCESS clusters, and the solid line represents their best fitting L_X - T_X relationship, which is notably similar to that of the RCS combined sample (dashed line).

Table 7. Scaling Relationship: $\log_{10} (E_z^{-1} L_X) = C_1 + C_2 \log_{10} T_X$

Sample	Bisector		Orthogonal	
	C_1	C_2	C_1	C_2
CNOC ^a	0.74 ± 0.08	2.3 ± 0.3		
RCS (high- z) ^a	0.36 ± 0.06	2.1 ± 0.3		
RCS (total)	0.34 ± 0.06	2.7 ± 0.5	0.34 ± 0.06	2.8 ± 0.5
REXCESS (disturbed)	0.43 ± 0.05	2.8 ± 0.7	0.5 ± 0.1	3.8 ± 0.6
REXCESS (ncc)	0.46 ± 0.03	3.2 ± 0.3	0.47 ± 0.03	3.4 ± 0.4
REXCESS (total)	0.63 ± 0.06	3.1 ± 0.3	0.68 ± 0.07	3.9 ± 0.5

^a [Hicks et al. \(2008\)](#)

5.4 Gas Mass Fractions

Using our estimated masses (Table 5) we calculate core gas mass fractions within R_{2500} . Our sample mean is $.058 \pm 0.008$ using Y_X to determine total mass (error computed by dividing the standard deviation by \sqrt{N}). In comparison, REXCESS clusters have a mean gas mass fraction of 0.081 ± 0.003 for the complete sample of 31 clusters, and 0.066 ± 0.004 when including only the 12 disturbed clusters; further evidence of similarities between optically selected clusters and morphologically disturbed X-ray selected clusters.

We perform statistical tests comparing the distributions of f_{gas} values for a subset of the clusters in our moderate redshift RCS sample with two subsets of the REXCESS sample. In order to compare clusters of similar masses, and to be consistent with Hicks et al. (2008), we restricted the temperature range in all 3 samples to be between 3.5–8.0 keV, resulting in 5 clusters from the RCS, 17 clusters in the REXCESS sample, and 7 clusters in the REXCESS/disturbed sample. The mean gas fraction and standard deviation from each of the subsamples are 0.050 ± 0.005 , 0.084 ± 0.004 , and 0.071 ± 0.005 , for the RCS subset, REXCESS subset, and REXCESS/disturbed subset respectively. The RCS subset shows lower f_{gas} than the REXCESS cluster subset, but similar f_{gas} to the REXCESS/disturbed cluster subset, also visible in the histograms shown in Figure 4.

We also performed a two-sided Kolmogorov-Smirnov test (the contributed KSTWO IDL routine, based on Press et al. 1992, Numerical Recipes), pairing the RCS subset with each of the REXCESS and REXCESS/disturbed subsets. The KS test comparing RCS clusters with the complete REXCESS sample showed a higher probability of having been randomly drawn from different parent populations than the test involving only the REXCESS/disturbed subsample; however, such a comparison is severely limited by the small number of clusters. The KS probability comparing the 5 RCS clusters with the 17 REXCESS clusters was 0.013, while the KS probability comparing the RCS clusters with 7 REXCESS/disturbed clusters was 0.091.

6 SUMMARY AND DISCUSSION

We have presented a detailed X-ray investigation of a sample of moderate-redshift, optically selected clusters of galaxies from the Red-sequence Cluster Survey (Table 1). All of our targets were detected by *Chandra* and/or *Suzaku* at $S/N > 11$ (Table 2) and were found within $27''$ of their optical positions. *Chandra* imaging reveals that most of these clusters possess at least some degree of substructure (Figure 1).

Surface brightness profiles were extracted for the seven *Chandra*-observed clusters in $S/N > 3$ annular bins. These profiles were reasonably well fitted by single β -models (Table 3 and Figure B1). Cluster emission was modeled with XSPEC, beginning with a spectral extraction region of 300 kpc radius. The results of single-temperature spectral fits (Table 4), combined with gas masses obtained using best-fit β -models, were used to determine Y_X and consequently R_{2500} . This process was carried out iteratively until extraction regions and R_{2500} estimates were in agreement.

Using both the $M-Y_X$ (Arnaud, Pointecouteau, & Pratt 2007) and $M-T_X$ relationship (Arnaud, Pointecouteau, & Pratt 2005), total masses were estimated out to R_{2500} . While both relationships are overall consistent within our errors, we find $M-Y_X$ mass estimates to generally be lower than those obtained via $M-T_X$ for the clusters in our sample, not entirely surprising given that $M-Y_X$ uses gas

mass information as well as temperature. Reassuringly, uncertainties in R_{2500} do not lead to large uncertainties in $L_X[R_{2500}]$. Therefore for X-ray observations for which only global T_X and L_X measurements are possible due to poor spatial resolution and/or low net counts, using $M-T_X$ to determine R_{2500} results in reasonably accurate L_X-T_X relationships. Values of R_{2500} , total mass, gas mass, gas mass fraction, and integrated luminosity are given in Table 5.

The scaled density profiles (Figure 2) and global quantities of the moderate-redshift RCS sample are most consistent with the morphologically disturbed subset of the REXCESS X-ray selected sample. These density profiles explain trends in L_X-T_X relationships (e.g., Figure 3; Hicks et al. 2008) without having to resort to non-standard evolutionary effects. This result suggests that much of the non-standard evolution found by previous work may be due to the varying fractions of cool cores in different samples, which in turn are affected by the various methods of cluster selection.

The properties of the scaled density profiles are reflected in the global quantities T_X and especially L_X , and vice versa. Low L_X systems have centrally-suppressed density profiles; high L_X systems have centrally-peaked density profiles. Trends in the L_X-T_X relation measured in an aperture corresponding to R_{2500} are similar to those measured at R_{500} (Pratt et al. 2009). cool-core systems populate the high- L_X side of the relation; morphologically disturbed systems populate the low- L_X side.

The fraction of cool-core clusters in the low-redshift RCS sample appears to be lower than in the REXCESS sample (1/7 versus 10/31). This lower fraction is consistent with the differences seen in density profiles and scaling relations. However, the small numbers and potential mismatch in mass distributions keep this discrepancy in cool-core fraction from being statistically significant. If there is an increase in the cool-core fraction towards the present day, there is a possibility that the percentage of cool cores found in X-ray and optically selected samples might converge at higher redshift. However, there are very few minimally-biased X-ray selected cluster samples that probe the redshift ranges we are interested in. The eROSITA survey (Predehl et al. 2011) will definitely shed light on this issue.

Overall we find that optically selected RCS cluster properties span the entire range of those of massive clusters selected via other methods, but contain a higher fraction of objects with gas density profiles and global properties similar to those of the morphologically-disturbed systems in REXCESS. This result suggests that optical and X-ray selection do not sample exactly the same population of clusters. Recent results from SZ surveys such as Planck (Planck Collaboration et al. 2011), further suggest that X-ray selection may preferentially pick up centrally-concentrated systems. Selection effects such as these have the potential to affect the interpretation of cluster surveys that intend to use the evolution of the cluster population as a proxy for cosmic evolution. More investigations are clearly necessary.

ACKNOWLEDGEMENTS

Support for this work was provided by the National Aeronautics and Space Administration through *Suzaku* Awards NNX08AZ72G and NNX10AH92G, and *Chandra* award GO9-0149 issued by the *Chandra* X-ray Observatory Center, which is operated by the Smithsonian Astrophysical Observatory for and on behalf of the National Aeronautics Space Administration under contract NAS8-03060. NSF AST-0206154 provided support for spectroscopic ob-

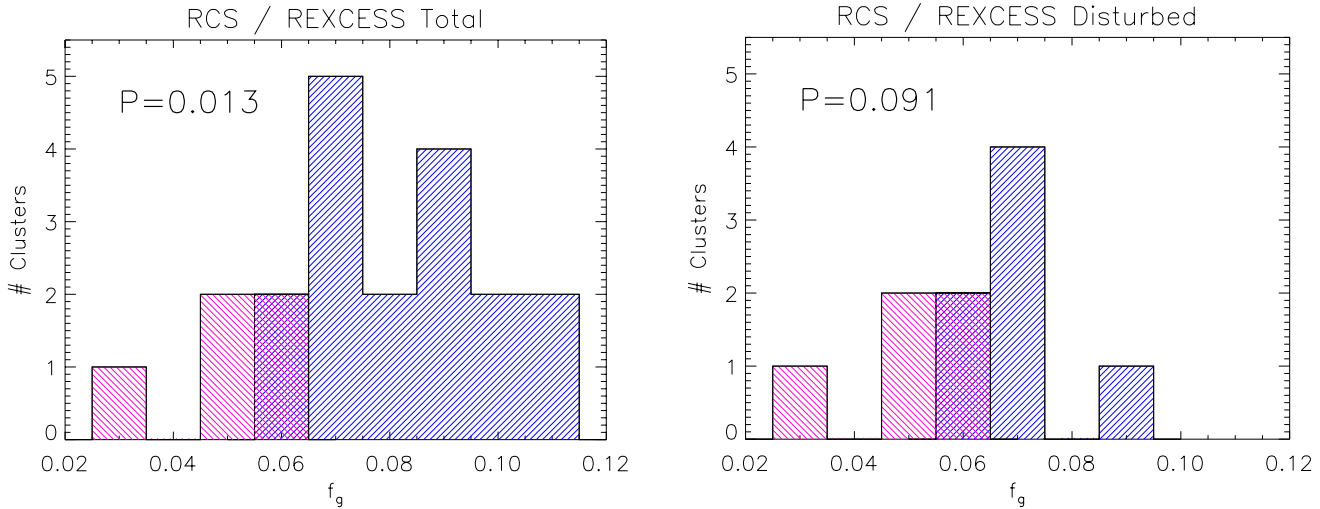


Figure 4. Gas Mass Fractions. *Left:* Histogram of gas mass fractions for the 5 moderate- z RCS and 17 REXCESS clusters with $3.5 < T_X < 8$ keV. A K-S test performed on these two samples resulted in $D=0.741$ and $P=0.013$, indicating that the gas mass fractions of the two samples are unlikely to have been drawn from the same distribution. *Right:* Using only the 7 disturbed REXCESS clusters with $3.5 < T_X < 8$ keV.

servations. Support for Megan Donahue and Amalia Hicks was also provided by LTSA award NNG05GD82G.

REFERENCES

- Abell, G. O. 1958, *ApJS*, 3, 211
- Allen, S. W., Evrard, A. E., & Mantz, A. B. 2011, *ARA&A*, 49, 409
- Arnaud, K.A. 1996, *ADASS*, 101, 5
- Arnaud, M., Pointecouteau, E. & Pratt, G.W. 2005, *A&A*, 441, 893
- Arnaud, M., Pointecouteau, E., & Pratt, G. W. 2007, *A&A*, 474, L37
- Akritis, M.G. & Bershad, M.A. 1996, *ApJ*, 470, 706
- Barger, A. J., Cowie, L. L., Mushotzky, R. F., et al. 2005, *AJ*, 129, 578
- Basilakos, S., Plionis, M., Georgakakis, A., et al. 2004, *MNRAS*, 351, 989
- Bautz, M., Miller, E., Arnaud, K., et al. 2007, *Progress of Theoretical Physics Supplement*, 169, 20
- Blindert, K. 2006, Ph.D. Thesis, University of Toronto
- Böhringer, H., Schuecker, P., Guzzo, L., et al. 2004, *A&A*, 425, 367
- Böhringer, H., Schuecker, P., Pratt, G. W., et al. 2007, *A&A*, 469, 363
- Böhringer, H., Pratt, G., Arnaud, M., et al. 2010, *A&A*, 514, A32
- Cash, W. 1979, *ApJ*, 228, 939
- Chatzikos, M. 2012, Ph.D. Thesis, University of Virginia
- Conconi, P., Campana, S., Tagliaferri, G., et al. 2010, *MNRAS*, 405, 877
- Content, R., Cimatti, A., Robberto, M., et al. 2008, *SPIE*, 7010
- Dickey, J.M. & Lockman F.J. 1990, *ARA&A*, 28, 215
- Donahue, M., Mack, J., Scharf, C., et al. 2001, *ApJL*, 552, L93
- Donahue, M., Scharf, C., Mack, J. et al. 2002, *ApJ* 569, 689
- Ellingson, E., Gilbank, D. G., Yan, R., Yee, H. K. C. & Gladders, M. 2012, in prep
- Ettori, S., Tozzi, P. & Rosati, P. 2003, *A&A*, 398, 879
- Gilbank, D.G., Bower, R.G., Castander, F.J. et al. 2004, *MNRAS* 348, 551
- Gioia, I.M., Henry, J.P., Maccacaro, T., Morris, S.L., Stocke, J.T., & Wolter, A. 1990, *ApJ*, 356, L35
- Gladders, M.D., Yee, H.K.C. 2005, *ApJS*, 157, 1
- Hicks, A.K., Ellingson, E., Yee, H.K.C., & Hoekstra, H. 2006, *ApJ*, 652, 232
- Hicks, A.K. et al. 2008, *ApJ*, 680, 1022
- Holden, B. P., Romer, A. K., Nichol, R. C., & Ulmer, M. P. 1997, *AJ*, 114, 1701
- Kravtsov, A. V., Vikhlinin, A., & Nagai, D. 2006, *ApJ*, 650, 128
- Lloyd-Davies, E. J., Romer, A. K., Mehrrens, N., et al. 2011, *MNRAS*, 418, 14
- Marriage, T. A., Acquaviva, V., Ade, P. A. R., et al. 2011, *ApJ*, 737, 61
- Nagai, D. 2006, *ApJ*, 650, 538
- Neumann, D. M., & Arnaud, M. 1999, *A&A*, 348, 711
- Planck Collaboration VIII. 2011, *A&A*, 536, A8
- Planck Collaboration, Aghanim, N., Arnaud, M., et al. 2011, *A&A*, 536, A9
- Pointecouteau, E., Arnaud, M. & Pratt, G.W. 2005, *A&A*, 435, 1
- Popesso, P., Böhringer, H., Brinkmann, J., Voges, W., & York, D. G. 2004, *A&A*, 423, 449
- Pratt, G. W., Croston, J. H., Arnaud, M., Böhringer, H. 2009, *A&A*, 498, 361
- Predehl, P., Andritschke, R., Becker, W., et al. 2011, *SPIE*, 8145
- Press, W. H. et al. 1992, “Numerical Recipes in C: The Art of Scientific Computing”, Cambridge University Press
- Sánchez, A. G., Lambas, D. G., Böhringer, H., & Schuecker, P. 2005, *MNRAS*, 362, 1225
- Šuhada, R., Song, J., Böhringer, H., et al. 2012, *A&A*, 537, A39
- Valtchanov, I., Pierre, M., Willis, J., et al. 2004, *A&A*, 423, 75
- Vanderlinde, K., Crawford, T. M., de Haan, T., et al. 2010, *ApJ*, 722, 1180
- Voit, G. M., & Donahue, M. 2005, *ApJ*, 634, 955
- Wester, W., & Dark Energy Survey Collaboration 2005, *Observing Dark Energy*, 339, 152
- Wilson, G., Muzzin, A., Yee, H. K. C., et al. 2009, *ApJ*, 698, 1943

- Xue, Y. & Wu, X. 2000, ApJ, 538, 65
 Yee, H. K. C., Ellingson, E., Abraham, R. G., Gravel, P., Carlberg, R. G., Smecker-Hane, T. A., Schade, D., & Rigler, M. 1996, ApJS, 102, 289
 Yee, H.K.C., Ellingson, E., & Carlberg, R.G. 1996, ApJS, 102, 269
 Yee, H.K.C., Lopez-Cruz, O. 1994, AJ, 117, 1985

APPENDIX A: SIGNAL-TO-NOISE RATIOS

To estimate the significance of RCS cluster detections in the X-ray, we used the same simple statistics as in [Hicks et al. \(2008\)](#). For the *Chandra* observed clusters, counts were extracted in the 0.3-7.0 keV band from a $500 h_{70}^{-1}$ kpc radius region around the X-ray peak (*C*) and also from a region away from the aimpoint on the same chip which served as a background (*B*). Due to the ~ 2 arcminute spatial resolution of *Suzaku*, all analysis was performed using a 260 arcsecond extraction radius, as recommended by the *Suzaku* Data Reduction Guide⁴. Therefore to determine S/N for our *Suzaku* observations, counts were extracted in the 0.2-12.0 keV band from a $260''$ radius region centered on the cluster (*C*), and the remainder of the chip minus calibration sources was used as the background (*B*). Obvious point sources were removed from each region in all observations. Final signal-to-noise ratios were calculated based on dividing net counts, $N = C - B$, by the standard deviation, $\sigma = \sqrt{C + B}$. Using this method, all clusters were solidly detected at a signal-to-noise ratio greater than 11 (Table 2), with an average S/N of 41 for the sample.

APPENDIX B: β MODEL FITS

⁴ <http://heasarc.nasa.gov/docs/suzaku/analysis/abc/>

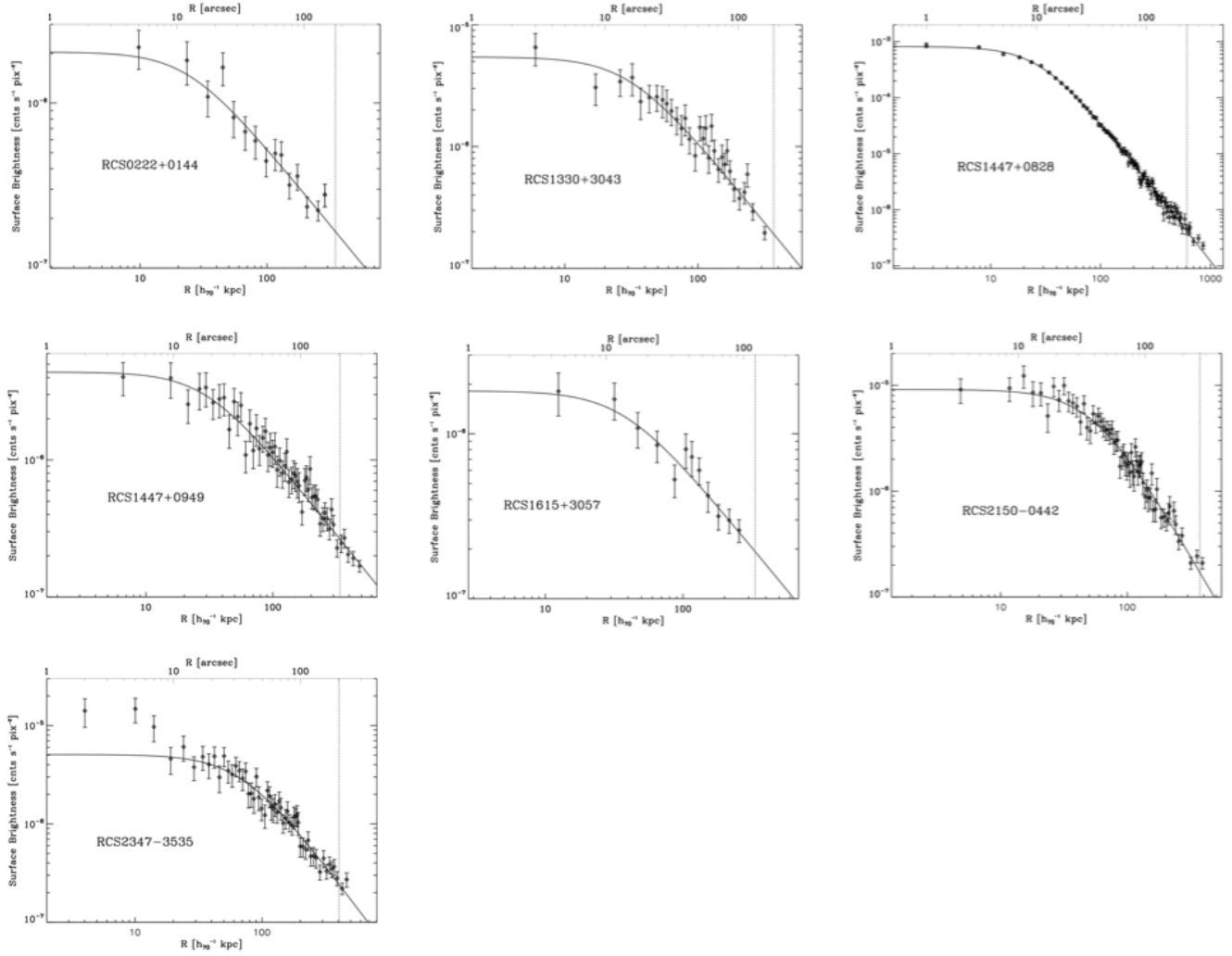


Figure B1. Surface Brightness Profiles. Background-subtracted radial surface brightness profiles for the 0.3–2.5 keV band accumulated in $S/N > 3$ annular bins for seven of the nine clusters in our sample. A solid line traces the best fitting single β model of each cluster. Vertical dashed lines indicate R_{2500} . Many of the profiles exhibit some substructure; however, most were reasonably well fitted by a standard β model (see Table 3 for goodness of fit data). The surface brightness profile of RCS2347-3535 suggests that it harbors a modest cool core in the inner 10–20 kpc.